Flexible and Stretchable Optical Waveguide Tactile Sensor for 3-Axial Force Sensing

Yue Li, Wenlong Gaozhang, Jian Hu, Gongyu Zhang, Prokar Dasgupta, Sebastien Ourselin and Hongbin Liu

***Abstract*—Tactile sensing is essential for precise manipulation and ensuring safety by providing real-time feedback on external forces and interactions. However, conventional tactile sensors struggle to maintain flexibility, accuracy, and reliability when applied to complex or flexible surfaces. To address these limitations, we present a novel, fully flexible optical waveguide sensor capable of 3-axial force sensing by detecting variations in light intensity within intersecting optical channels. This work includes a comprehensive theoretical analysis and modeling of optical waveguide mechanisms, focusing on intrinsic, extrinsic, and intersection losses, thereby establishing a foundation for optimizing sensor design and minimizing these losses. The sensor's performance was validated through experiments involving various deformation modes, including stretching, bending, and pressing, achieving a resolution of 0.0073 N and a hysteresis of 4.76%. To model the relationship between applied forces and light intensity loss, we employed an artificial neural network, which achieved an error margin of 0.10058 N (R^2 = 0.98472) in force prediction. The combination of high performance, flexibility, and accuracy makes this sensor a promising solution for tactile sensing in advanced applications such as flexible systems and soft robotics.**

***Index Terms*—Flexible tactile sensing, 3-Axial force sensor, Haptic interface, Soft robotics.**

I. Introduction

TACTILE sensing which involves the ability to accurately perceive and respond to external stimuli, is essential for precise manipulation and improved safety in various applications, including biomedical devices, wearable technologies, and robotics [1]. However, traditional tactile sensors often encounter difficulties i n m aintaining p erformance a nd reliability when applied to flexible s tructures o r c omplex surface geometries [2]. To overcome these challenges, flexible tactile sensing technologies have emerged as a promising solution, providing the adaptability and sensitivity needed to function effectively in dynamic and complex environments.

Currently, researchers are investigating various approaches to developing flexible force sensors based on resistive [3]–[5], capacitive [6]–[9], piezoelectric [10]–[13], and triboelectric technologies [14]–[17]. Although these electrical-based sensors exhibit high sensitivity and provide straightforward readouts [18], they often suffer from poor biocompatibility and are highly susceptible to electromagnetic interference [19]. In contrast, soft optical-waveguide-based tactile sensing has distinct advantages of compact size, inherent electrical safety, and immunity to electromagnetic interferences [20].

Optical waveguide-based tactile sensors utilize light signals, including variations in wavelength and intensity, to detect deformations caused by external environmental factors [19]. One of the earliest and most widely studied approaches involves the integration of Fiber Bragg Gratings (FBGs) into flexible substrates, such as silicone or polydimethylsiloxane (PDMS), which allows the precise tactile sensing through the analysis of wavelength shifts in the reflected light as the fiber deforms under applied forces [21]–[23].

While FBG-based tactile sensors have demonstrated remarkable effectiveness in detecting subtle deformations and demonstrate excellent sensitivity to external forces [24]–[26], a significant limitation is their inability to fully conform to highly deformable substrates. This lack of compliance can result in mechanical failures, such as delamination or fiber breakage, especially under conditions of repeated or extreme bending, stretching, or torsional forces [27]. Additionally, FBG systems require costly demodulation equipment, which poses economic challenges and restricts their accessibility for broader applications [28].

To address these limitations, recent research has focused on developing optical waveguide sensors that utilize light intensity as a variable for tactile sensing. A commonly adopted strategy involves the use of polymers, such as PDMS, as optical waveguides, which are typically embedded with emitters and photodetectors to enable efficient force detection [29], [30]. This innovative approach has demonstrated exceptional sensitivity, achieving impressive performance metrics, including a sensitivity of up to $0.2\,\mathrm{kPa}^{-1}$ in the low-pressure regime (less than 1 kPa) [31] and a weight sensitivity of $0.193\,\mathrm{g}^{-1}$ [32].

Building on these advancements, researchers have investigated multimodal deformation sensing to detect various deformation modes, including bending, stretching, and pressure, thereby enhancing understanding of how external forces interact with sensors. A notable development is the stretchable

This work was supported by InnoHK program. The work of Yue Li was supported by China Scholarship Council under CSC NO. 202006280025. *(Corresponding author: Yue Li)*

Yue Li is with the Department of Computer Science, University College London, London, WC1E 7JE, UK (e-mail: yue-li@ucl.ac.uk).

Wenlong Gaozhang is with the School of Computer Science and Electronic Engineering, University of Essex, Colchester, CO4 3SQ, UK (e-mail: wenlong.gaozhang.20@essex.ac.uk).

Jian Hu, Hongbin Liu are with Chinese Academy of Sciences, Institute of Automation (CASIA), Beijing, China and the Centre of AI and Robotics (CAIR), Hong Kong Institute of Science & Innovation, Chinese Academy of Sciences, Hong Kong, China (e-mail: hujian@ia.ac.cn; liuhongbin@ia.ac.cn).

Gongyu Zhang is with the School of Biomedical Engineering & Imaging Sciences, King's College London, London, SE1 7EH, UK (e-mail: gongyu.zhang@kcl.ac.uk).

Prokar Dasgupta and Sebastien Ourselin are with MRC Centre for Transplantation, NIHR Biomedical Research Centre, King's College London, and Guy's and St. Thomas' NHS Foundation Trust, Urology, London, UK (e-mail: prokar.dasgupta@kcl.ac.uk; sebastien.ourselin@kcl.ac.uk).

optical waveguide sensor featuring a semi-divided optical core that enables two-degree-of-freedom strain sensing, allowing it to effectively detect and differentiate between multiple modes of deformation such as elongation, bending, twisting, and local pressure, by analyzing changes in optical power throughput [33]. To further improve the decoupling of deformation modes, Heiden et al. [34] and Zhao et al. [35] achieved multimodal detection and differentiation through an integrated optical waveguide network that distinguishes the output response patterns for various deformations. Recently, Bai et al. [36] designed a stretchable distributed fiber optic sensor (DFOS) utilizing elastomeric lightguides with chromatic patterns. This innovative sensor effectively differentiates between stretching, bending, and pressing, demonstrating a strain sensitivity of 2 to $5\,\mathrm{dB\,e^{-1}}$ over 150% elongation and a pressing sensitivity of 0.9 to $1.2\,\mathrm{dB\,N^{-1}}$ for 2 to $5\,\mathrm{N}$ forces.

Despite these significant advancements, existing approaches are still predominantly focused on the detection of normal forces [37], [38], leaving a critical gap in the effective measurement of tangential forces, which are crucial for tasks requiring delicate handling, precise manipulation, and safe interactions. Although recent studies [39], [40] have proposed flexible optical sensors capable of effective slip detection, they are primarily applicable to near flat surfaces, limiting their use on complex and curved geometries.

Overall, there remains a pressing need for innovative solutions capable of accurately measuring 3-axial forces within flexible optical waveguides while ensuring optimal sensor performance under varying deformations. In our previous research, we proposed a novel and compact optical-based 3-axial force sensor designed for surgical forceps. This sensor detects both the magnitude and direction of applied forces by analyzing light intensity patterns from three intersecting channels, specifically measuring the disruption of total internal reflection (TIR) [41]. However, the proposed sensor incorporates rigid components, such as the supporting base and the protective cover, limiting its ability to stretch or bend. Additionally, the shape of the force sensor must be customized for different applications.

To address these limitations and advance the frontier of tactile sensing, this paper presents a fully flexible force sensor with 3-axial sensing capability that can adapt to curved and complex surfaces. Our contributions are:

- Presents a comprehensive analysis and theoretical modeling of the fundamental principles of optical waveguides, focusing on the mechanisms of light loss under various deformation modes, including bending, stretching, and pressing. Additionally, a quantitative assessment using an optical geometric model is provided to evaluate intersection losses, establishing a theoretical foundation for optimizing waveguide designs to minimize light loss in complex applications. (see Section II-A.
- Develops a flexible 3-axial optical waveguide sensor that adapts to various curved and complex surfaces, achieving a resolution of 0.0073 N and a hysteresis of 4.76% while utilizing a neural network for precise force prediction with an error margin of only 0.10058 N, demonstrating its high performance in complex environments. (see Section II-B and III-C).
- Demonstrates the sensor's performance across various deformation modes, including stretching, bending, and pressing, thereby confirming its reliability for enabling effective 3-axial force sensing in flexible devices and soft robotics. (see Section III-A and III-B).

Section II delves into the working principles of the optical waveguide, addressing intrinsic, extrinsic, and intersection losses. The section also covers the detailed design and fabrication process of the sensor, providing a comprehensive understanding of its construction and functionality. Section III describes the experimental scenarios and platforms employed to evaluate the sensor's performance. It offers a thorough assessment of both single and combined deformation modes. The characterization of the sensor is discussed in detail, and a data-driven neural network is utilized to predict external forces. The conclusion and discussion are in Section IV.

II. SENSOR DESIGN

A. Working principle of the optical waveguide

Typically, an optical waveguide consists of a core with a high refractive index n_1 surrounded by a cladding with a lower refractive index n_2, as illustrated in Fig. 1(a). Light propagates

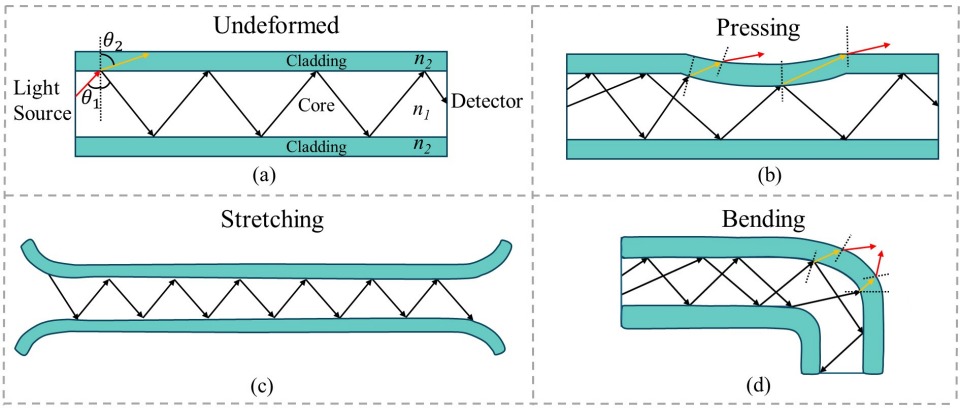

Fig. 1. Working principle of the optical waveguide: (a) Light propagates within the waveguide based on the principle of total internal reflection(TIR). (b) Ray diagrams of the waveguide when it is pressed, (c) stretched, and (d) bent.

within the waveguide based on the principle of total internal reflection (TIR), which occurs when the angle of incidence θ_1 exceeds the critical angle ϕ [42]. The critical angle ϕ is given by:

$$\phi = \sin^{-1}\left(\frac{n_2}{n_1}\right) \tag{1}$$

In this configuration, the core effectively confines the light, allowing it to propagate along the length of the waveguide with minimal loss. However, as light travels through the optical waveguide, various mechanisms can contribute to its attenuation, which can be broadly classified into intrinsic and extrinsic losses.

1) Intrinsic losses: Intrinsic losses are inherent to the material and structural properties of the waveguide. These losses primarily include absorption and scattering [43]. To quantitatively characterize the intrinsic optical loss, the exponential attenuation coefficient is typically employed. The intensity (power per unit area) at any point along the length of the waveguide can thus be described by [44]:

$$I(x) = I_0 e^{-\alpha x} \tag{2}$$

where $I(x)$ represents the light intensity at point x along the waveguide; I_0 is the initial light intensity at the starting point of the waveguide (i.e., when $x = 0$); α is the attenuation coefficient.

2) Extrinsic losses: Extrinsic losses in optical waveguides are induced by various physical deformations, including stretching, bending, and pressing. These external factors disrupt the waveguide's structural integrity, thereby impacting light propagation and leading to power loss. Fig. 1 illustrates the variations in light paths within the waveguide under different deformation modes.

Pressing: When the optical fiber is pressed, TIR is no longer satisfied, as illustrated in Fig. 1(b). The pressing causes light to couple from guided modes to radiation modes, resulting in part of the light escaping through the core and passing into the cladding due to deformation, leading to light loss. Assuming the optical waveguide forms an arc shape under the applied force, the geometric characteristics of the arc can be described as follows:

$$m = R\varphi \tag{3}$$

where m represents the arc length, φ represents the central angle of the arc, and R represents the radius of the arc. Assuming the waveguide is a linear elastic material, the deformation radius R is inversely proportional to the applied force F, given by:

$$R = \frac{k}{F} \tag{4}$$

where k is the stiffness of the waveguide. Given that light loss is proportional to the reciprocal of the bending radius R and that a larger applied force F results in a smaller bending radius R, it follows that the optical loss is directly proportional to the applied force F.

Stretching: As shown in Fig. 1(c), when the optical waveguide undergoes stretching, its physical length increases, according to the Beer-Lambert Law [45]:

$$A = \epsilon c l \tag{5}$$

where A is the absorbance of light, l is the path length, ϵ is the absorptivity of the material, and c is the concentration of chemical species in the medium that attenuate light. Given this relationship, as the path length l increases during stretching, and with ϵ and c remaining constant, the optical loss (absorbance) increases proportionally.

Bending: When an optical fiber bends, as illustrated in Fig. 1(d), the bending reduces the incidence angle of light at the core-cladding interface below the critical angle required for TIR. This failure of TIR results in light leakage from the core into the cladding and subsequently into the surrounding environment.

According to Eq.2, the attenuation of light intensity I over a propagation distance x in a fiber, characterized by an attenuation coefficient α exhibits an exponential decay trend. Regarding bending loss, Snyder et al. [46] introduced the concept that the emitted light intensity at the bend also decays exponentially but with a different attenuation coefficient β, which varies with the bending radius:

$$I(x) = I_0 e^{-\beta x} \tag{6}$$

$$\beta = a_1 e^{-a_2 R} \tag{7}$$

where a_1 and a_2 are constants dependent on the dimensions and geometry of the waveguide. The coefficient β exhibits an exponential relationship with the radius of curvature R.

3) Intersection losses: In addition to internal and external light losses, intersection losses in complex structured optical waveguides are significant and cannot be ignored. When two optical waveguides intersect, a portion of the propagating light in each guide may leak into the other waveguide or dissipate into the surrounding environment [47].

As illustrated in Fig. 2(a), the intersection involves two waveguides crossing at an angle α with each waveguide having a width of $2d$. The refractive indices of the core and cladding are n_1 and n_2, respectively. The incident rays are characterized by the angle θ relative to the center axis and by the distance x from the center axis along the AD line. Here, the angle θ is complementary to the incident angle θ_1.$\theta > 0$ indicates that the incident ray is directed upwards from the center axis of the waveguide, while $\theta < 0$ indicates that the incident ray is directed downwards from the center axis. The critical conditions for light leakage at the intersection are illustrated in Fig. 2(a), where

$$s = AB = \frac{2d}{\tan\alpha} \tag{8}$$

$$l = BC = CE = ED = DB = \frac{2d}{\sin\alpha} \tag{9}$$

When $\theta > 0$,

$$\frac{d-x}{s+l} < \tan\theta < \frac{d-x}{s} \tag{10}$$

When $\theta < 0$,

$$\tan\theta < -\frac{d+x}{l} \tag{11}$$

To quantitatively analyze the relationship between intersection loss and the intersecting angle, we conducted an analysis

based on geometric optics, as shown in Fig. 2(b), which illustrates a 2D conceptual diagram representing the angular and positional conditions (x, θ) under which light rays escape the waveguide core due to insufficient total internal reflection. Combining the conditions for total internal reflection as described in Section II.A, the angle θ satisfies the following constraints:

$$-d < \theta < d \tag{12}$$

$$-\cos^{-1}\left(\frac{n_2}{n_1}\right) < \theta < \cos^{-1}\left(\frac{n_2}{n_1}\right) \tag{13}$$

Assuming that the incident rays are homogeneous and uniformly distributed, then the leaking ratio L can be determined by calculating the proportion of the shaded area:

$$\begin{aligned} L = \frac{I_{\text{leak}}}{I_o} &= \frac{\int\int F(x,\theta)\,dx\,d\theta}{\int_{-\cos^{-1}\left(\frac{n_2}{n_1}\right)}^{\cos^{-1}\left(\frac{n_2}{n_1}\right)} \int_{-d}^{d} F(x,\theta)\,dx\,d\theta} \\ &= \frac{-\ln\left|\cos\left(\cos^{-1}\left(\frac{n_2}{n_1}\right)\right)\right|}{\cos^{-1}\left(\frac{n_2}{n_1}\right)} \cdot \frac{1}{\sin\alpha} \end{aligned} \tag{14}$$

It can be inferred that the light leakage ratio L at the crossing is inversely proportional to $\sin\alpha$ and remains unaffected by the waveguide's geometry, such as its width or length. As the crossing angle increases from 0° to 90°, the light leakage decreases correspondingly. Consequently, the light leakage is minimized at a crossing angle of 90°.

B. Sensor design

To achieve 3-axial force sensing, we have developed a fully flexible, fiber optic-based tactile sensor, shown in Fig. 3. This sensor consists of an integrated LED, four intersecting optical fibers, a sensing unit, photodiodes, a flexible base, and a protective cover. As detailed in Section II.A, the intersection angle of the four waveguides is optimized at 90° to minimize intersection losses.

3-axial force sensing is achieved by detecting distinct output patterns from the four channels. The LED emits light that propagates towards the input and subsequently divides into four channels. When external forces are applied to the sensing area from various directions, the corresponding sensor channels exhibit different responses, as summarized in Table 1. Specifically, under the application of a normal force, the sensing unit expands uniformly, leading to a uniform attenuation of light intensity across all channels. In contrast, when a tangential force is applied, the sensing unit undergoes asymmetric deformation, resulting in varied light intensity output patterns across the channels. This principle enables the measurement of both the magnitude and direction of the 3-axial force.

TABLE I
WORKING PRINCIPLE OF THE PROPOSED SENSOR

Force Direction	Force Vector (x, y, z)	Corresponding Channel
	(0,0,-1)	1, 2, 3, 4
	(0,1,-1)	1, 3
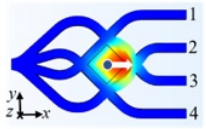	(1,0,-1)	2, 3
	(0,-1,-1)	2, 4
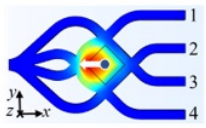	(-1,0,-1)	1, 4

C. Fabrication process

The fabrication process, as illustrated in Fig. 4, begins with creating the soft base and cover using Smooth Sil™960 (60A), a silicon-based elastomer. The material is mixed at a 10:1 (A:B) ratio and stirred for 3 minutes, followed by vacuum degassing to eliminate air bubbles. The degassed mixture is

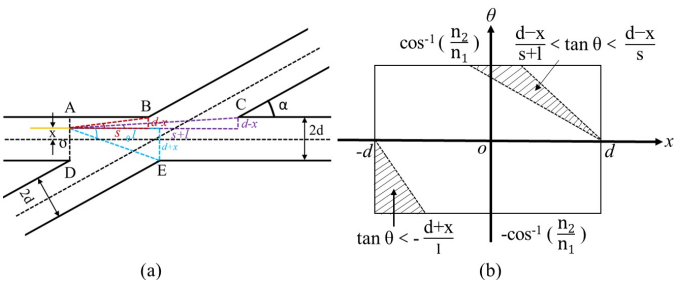

(a) (b)

Fig. 2. Analysis of light loss at the intersection: (a) Illustration of the critical conditions under which leakage occurs. (b) Calculation of light loss using principles of geometric optics.

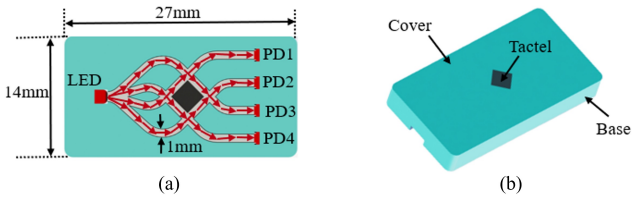

(a) (b)

Fig. 3. Layout of the proposed sensor: (a) The optical path of the waveguide. (b) The proposed sensor comprises an integrated LED, four intersecting optical fibers, a sensing unit, photodiodes, a flexible base, and a cover.

then injected into CNC-printed molds using a syringe and cured for 16 hours before demolding, as shown in Fig. 4(a).

Subsequently, the cladding layer is formed by spin-coating Ecoflex 00-50, with a refractive index of 1.40, onto the inner surfaces of both the base and cover (Fig. 4(b)). After curing for 3 hours, the cladded base and cover are positioned in a fixed mold and secured with screws, as depicted in Fig. 4(c). Clear Flex 30, with a refractive index of 1.47, is then prepared by mixing at a 1:1 (A:B) ratio and injected into predefined channels to form the core of the waveguide, followed by curing for 16 hours.

Once the core material is cured, the fixed mold is removed. A tactle layer made of Dragon Skin 20, with added black dye, is then injected over the designated sensing area and cured for 4 hours.

Finally, LEDs and photodiodes are assembled onto the flexible base, completing the sensor fabrication, as illustrated in Fig. 4(e). Throughout the process, all silicone materials underwent vacuum degassing post-mixing to ensure the removal of air bubbles. Detailed properties of the selected silicone materials and the specific processing steps are summarized in Table 2.

III. Experimental Scenarios and Platforms

To validate the sensor's performance, a series of experiments were conducted under various deformation conditions. Initially, the sensor underwent single-mode deformation tests, encompassing independent scenarios of stretching, bending, and pressing. Subsequently, combined deformation mode experiments were performed, which involved pressing tests conducted under varying bending curvatures and elongation states. Additionally, the sensor's performance was evaluated while simultaneously subjected to bending and stretching.

Throughout this process, light attenuation was quantified by:

$$a = 10 \log_{10} \left(\frac{I_0}{I} \right) \tag{15}$$

where I_0 represents the initial light intensity measured in the absence of bending, elongation, and pressing deformation, and I represents the output light intensity of each channel.

A. Single deformation modes

1) Stretching: Initially, the sensor was stretched over 20 times to mitigate the Mullins effect, which is characterized by softening and increased hysteresis observed in elastomeric materials during cyclic loading. For the stretching experiment, the sensor was clamped at both ends using two fixtures. One end was fixed to a stationary mount, while the other was connected to a precision micrometer translation stage (Thorlabs DRV001), enabling controlled horizontal displacement, shown in Fig. 5(a). The sensor is held using rigid plates and evenly distributed fastening screws to ensure uniform pressure and prevent slippage or asymmetric deformation during stretching. To minimize the potential influence of the clamping mechanism on the optical signals, the clamped region is confined to the ends of the waveguide, outside the sensitive sensing area. Additionally, the central segment of the sensor, where deformation and light transmission are measured, remains fully exposed and unencumbered by the fixtures. The sensor was gradually stretched to 40% elongation, with measurements taken at 10% increments while the intensity change of the four channels were continuously monitored during this process. This procedure was repeated five times and the output intensity under different elongation was obtained by averaging the collected data.

Fig. 5(a) depicts the relationship between light loss (dB) and elongation (%) for four channels during the tensile test. As the elongation increases from 0% to 40%, the light loss for each channel demonstrates a linear increase. Notably, the magnitude of change varies across the channels, which can be attributed to inaccuracies during the manufacturing process. Channel 4 exhibits the highest light loss, reaching approximately 4dB at 40% elongation, followed by Channel 2, Channel 1, and Channel 3.

2) Bending: Fig. 5(b) illustrates the bending test platform, which consists of modular fixture units designed to apply varying curvature to the sensor. Each fixture module includes a fixed base and a matching upper arc-shaped clamping block with an integrated slot. The sensor is inserted into this slot, which precisely guides and maintains the intended curvature. The upper and lower parts are secured using corner-mounted screws, ensuring stable fixation and preventing lateral movement. Notably, the slot in the arc-shaped clamp is designed

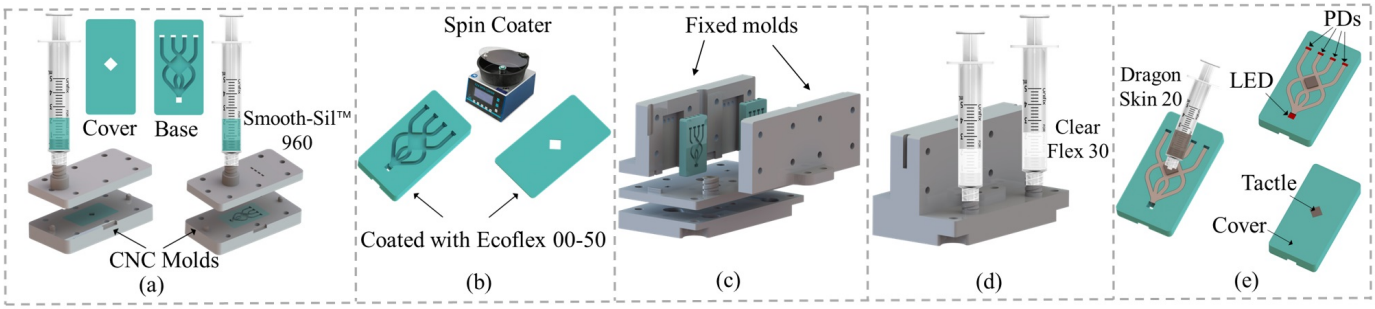

Fig. 4. Fabrication process of the proposed sensor: (a) Creation of the soft base and cover using Smooth Sil™ 960, and cured for 16 hours in CNC-printed molds. (b) Formation of the cladding layer by spin-coating Ecoflex 00-50, followed by a 3-hour curing period. (c) Positioning of the cladded base and cover in a fixed mold, secured with screws. (d) Injection of Clear Flex 30 to form the waveguide core, with a subsequent 16-hour curing. (e) Application of a tactile layer made of Dragon Skin 20 over the sensing area, cured for 4 hours, and final assembly of LEDs and photodiodes.

TABLE II
PROPERTIES OF SELECTED SILICONE MATERIALS

	Smooth-Sil™ 960	Ecoflex 00-50	Clear Flex 30	Dragon Skin 20
Mix ratio A:B	10:1	1:1	1:1	1:1
Mixing time	3 mins	3 mins	3 mins	3 mins
Curing time	16 h	3 h	16 h	4 h
Hardness	60A	00-50	30A	20A
Elongation	270%	980%	675%	620%
Colour	Green	Translucent	Clear	Translucent
Refractive index	/	1.40	1.49	1.41

with an open window above the sensing region, so no force is applied directly on the optical core. Mechanical clamping is applied only at both ends and the lateral edges of the sensor. This design ensures that the central sensing region remains suspended and uncompressed, minimizing any influence from the fixture on optical transmission. The sensor is subjected to various bending radii, from flat to 15 mm, 30 mm, 45 mm, and 60 mm, while the optical loss across four channels is monitored throughout the process. This measurement was repeated five times for each bending radius to ensure accuracy and repeatability.

Besides, Fig. 5(b) shows the relationship between light loss (dB) and curvature (mm^{-1}) for the four channels during the bending test. The results indicate a near-linear increase in light loss with increasing curvature, primarily attributed to the surface roughness of the sensor, which plays a critical role in its bending behavior. Rough surfaces cause irregular mode coupling, leading to higher losses that are not accurately predicted by macro bending theories, which generally assume a smooth and continuous surface. When the surface is rough, additional scattering losses are introduced, resulting in higher actual losses than those predicted by macro bending models.

3) Pressing: Fig. 5(c) shows the experimental setup for the pressing experiments. The sensor is rigidly clamped at both ends while the central sensing area remains fully exposed through an open window in the clamp, ensuring mechanical stability without inducing deformation, and the entire fixture is mounted on a stable base to eliminate platform-induced displacement. The 3-axis displacement platform (Oumeifar, LD40-LM) directed the external force to the sensor's tactel through a force indenter, and the applied force was accurately measured by a Nano 17 force sensor (Nano17-E, ATI Inc.), positioned behind the force indenter to serve as the force reference. To minimize slip between the force indenter and the

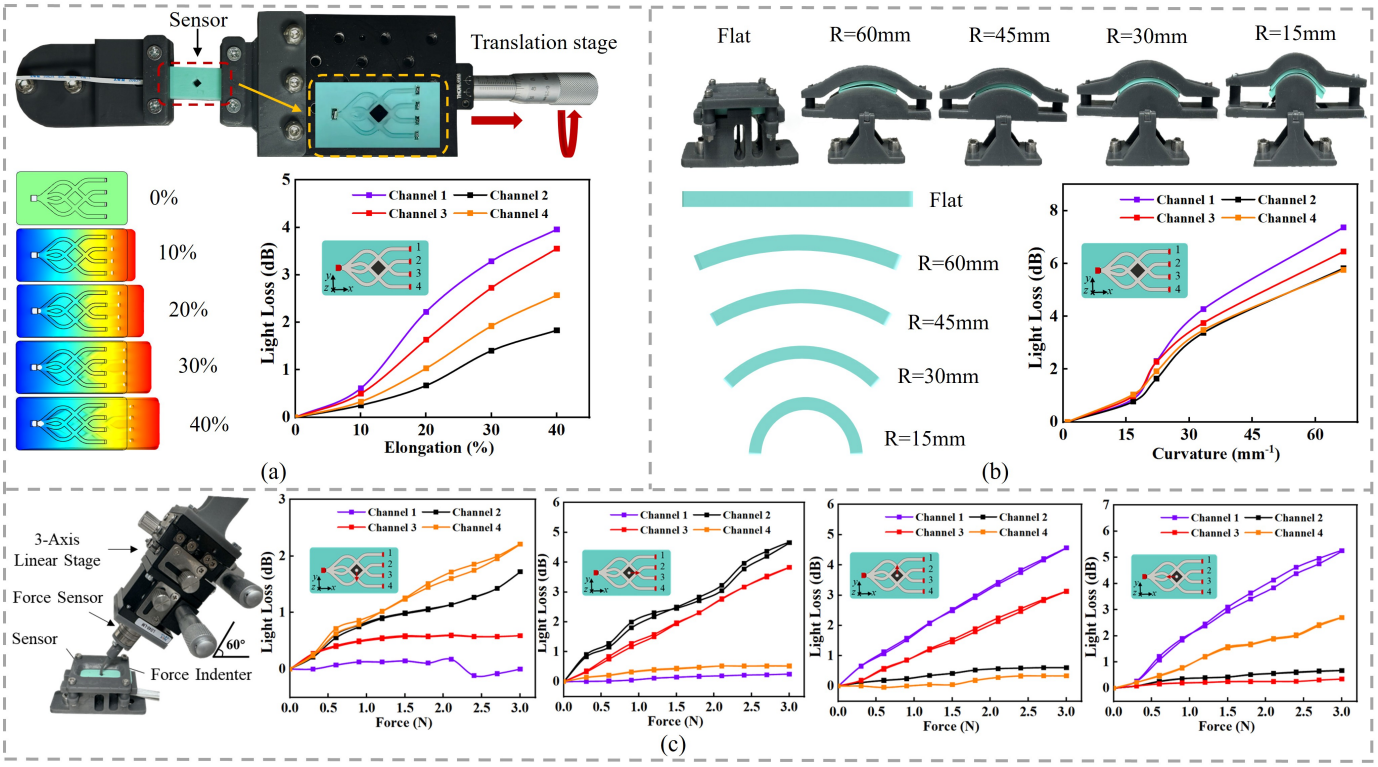

Fig. 5. Experimental setups and results for the waveguide under single deformation scenarios: (a) Stretching experiment setup and the relationship between light loss (dB) and elongation (%). (b) Bending experiment setup and the relationship between light loss (dB) and bending curvature(mm^{-1}). (c) Pressing experiment setup and the relationship between light loss (dB) and the applied force (N) from various directions.

sensor during loading and unloading, the indenter and sensor were pre-aligned and pressed into slight preload contact to create a stable contact interface that resists lateral movement. The output light intensity of the sensor was collected by light sensors (OPT4001) at the end of each channel and transmitted to a PC via Arduino for subsequent data analysis. The pressing test comprised both loading and unloading process and was repeated five times . During the pressing process, the 3-axis displacement platform and sensor were aligned at a fixed 60° angle. The applied force, comprising both normal and shear components, was systematically directed against the tactel across a 360° rotation.

The results are depicted in Fig. 5(c), which shows the light loss (dB) as a function of the applied force (N) for each channel. When the force was applied downward, Channels 2 and 4 exhibited the highest light loss, indicating that these channels were most affected by compression in this direction, while Channels 1 and 3 showed negligible changes. As the force direction changed to the right, Channels 2 and 3 exhibited the highest light loss, highlighting their sensitivity to forces from this direction. Conversely, when the force was applied upward, Channels 1 and 3 demonstrated the biggest light loss. Finally, when the force was directed to the left, Channels 1 and 4 exhibited the highest light loss. These results indicate that different channels are more responsive to forces from specific directions, which is crucial for the sensor's ability to detect 3-axial forces.

B. Combined deformation modes

To accurately assess the sensor's ability to detect external forces across various surfaces, it is essential to evaluate its performance under simultaneous deformation conditions. Fig. 6(a) and 6(b) illustrate the sensor's response to different curvatures and elongations, respectively. It is evident that under different bending curvatures and elongation, the sensor's performance and response trends are consistent with those observed during single pressing modes when external forces were applied from various directions. Notably, a larger bending curvature of the sensor results in a smaller light loss in the corresponding channels under the same applied force, which suggests that as the sensor bends more, a significant portion of the total light loss is attributed to the bending itself and the light loss due to the applied force becomes less significant in comparison. Similarly, the larger the elongation of the sensor, the smaller the light loss of the corresponding channels under the same applied force.

In practical applications, sensors often encounter simultaneous stretching and bending. To assess sensor performance under these combined deformation modes, two experimental sets were conducted, shown in Fig. 7(a). The sensor was clamped at both ends on a custom-designed platform with predefined curvature grooves while a micrometer translation stage applied horizontal elongation by pulling the right fixture. The first experiment involved a 20% elongation with a bending radius of 15mm, while the second involved a 40% elongation with a bending radius of 30mm. Light loss measurements for each channel were recorded under various directional forces. The results, as illustrated in Fig. 7(b) and Fig. 7(c), demonstrate a consistent pattern in channel response that parallels the behavior observed under the single pressing mode. This consistency highlights the sensor's adaptability to diverse shapes and surfaces, thereby enhancing its capability to accurately detect external forces across three axes.

C. Sensor characterization

1) Hysteresis: Hysteresis is commonly used to describe the inconsistency in a sensor's output during loading and unloading cycles. This phenomenon occurs because the sensor's soft material requires a certain amount of time to return

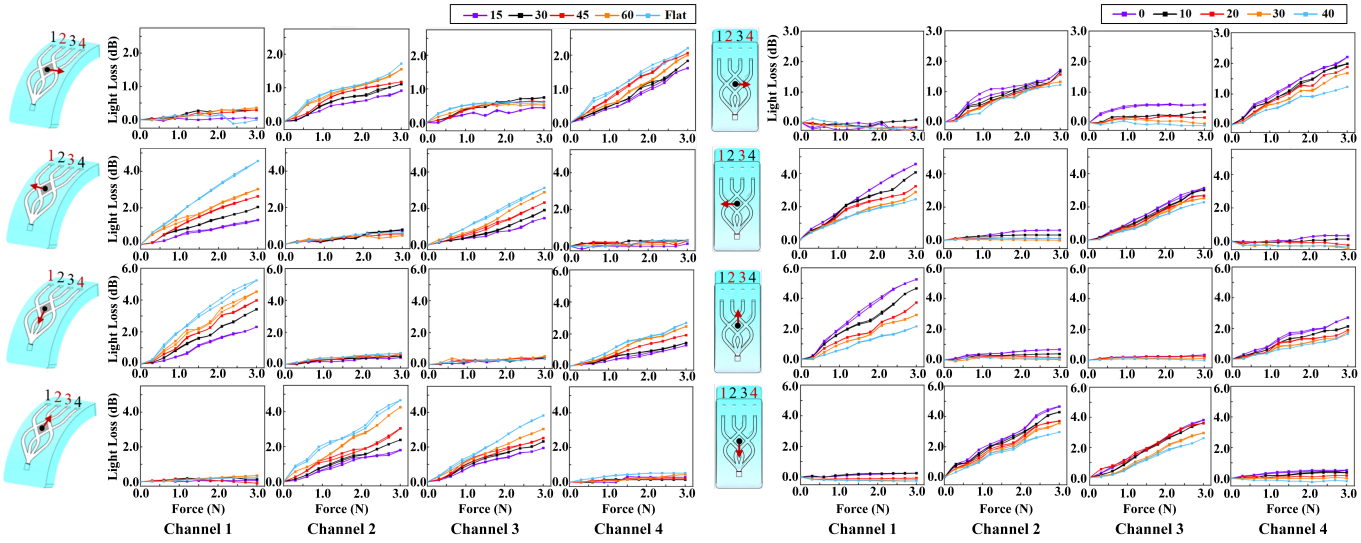

Fig. 6. Evaluation of sensor performance under simultaneous deformation scenarios: (a) Sensor response to varying bending curvatures, showing consistent trends with single pressing modes. Increased curvature results in reduced light loss under the same forces. (b) Sensor response to different elongations, where larger elongation decreases light loss in corresponding channels under the same force.

to its original, undeformed state after being deformed. To quantitatively analyze hysteresis, it can be calculated by [20]:

$$H = \frac{\Delta I_{\max}}{I_{FS}} \times 100\% \tag{16}$$

$$\Delta I_{\max} = \left[\overline{I_{unl,i}} - \overline{I_{loa,i}}\right]_{\max} \tag{17}$$

Where $\overline{I_{unl,i}}$ and $\overline{I_{loa,i}}$ represent the light loss during unloading and loading, respectively, I_{FS} is the full range output. The calculated results indicate that the maximum offset $\Delta I_{\max}$ is 0.25db and the average hysteresis error for the proposed sensor is 4.76%.

2) Resolution: The resolution of the sensor represents the minimum force that can lead to a change in the sensor's output light intensity. To identify the resolution, the baseline light intensity without any applied force was recorded to determine the noise level. Then, external forces were systematically applied and the changing light intensity for each increment was recorded. The smallest force that consistently produces a light intensity change above the noise threshold was determined to be 0.0073 N, which is the resolution of the sensor.

3) Repeatability: Repeatability is defined as the extent of variation in the measured output light intensity when force is applied from the same direction and it could be calculated by [20]:

$$R = \sqrt{\frac{1}{n-1}\sum_{i=1}^{n}(I_i - \overline{I})^2} \tag{18}$$

Where n is the number of measurements, I_i represents the light loss from the i-th measurement, and $\overline{I}$ is the average light loss. The repeatability for the four sensing units is 1.371%, 1.652%, 1.987%, and 1.689%, respectively.

D. Data-driven force sensor prediction neural network

To quantitatively describe the relationship between force and light intensity for the designed sensor under various deformation modes, we employed the neural network method to train the data collected from multiple deformation scenarios, thus enabling the estimation of external forces.This data-driven approach was chosen due to the nonlinear and coupled nature of optical signal responses under complex mechanical

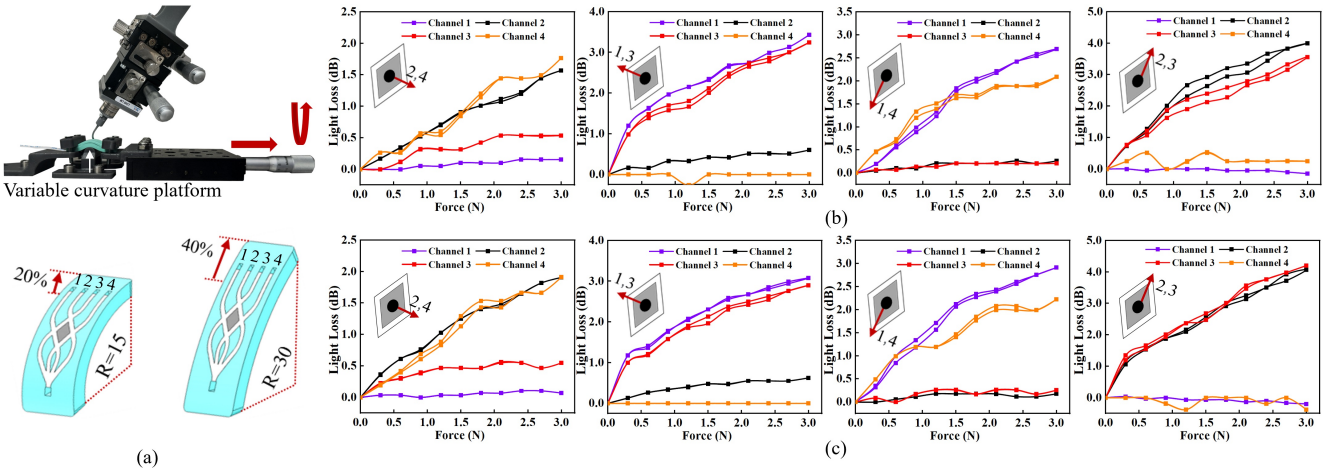

Fig. 7. Sensor performance during pressing experiments with simultaneous stretching and bending: (a) Experimental setups for two scenarios: 20% elongation with a 15 mm bending radius, and 40% elongation with a 30 mm bending radius. (b) Light loss measurements corresponding to the 20% elongation with a 15 mm bending radius. (c) Light loss measurements for the 40% elongation with a 30 mm bending radius. Results across channels under various directional forces exhibit consistent response patterns, paralleling behaviors observed in single pressing modes, thus underscoring the sensor's adaptability to conform to diverse curved surfaces curved surface for force detection.

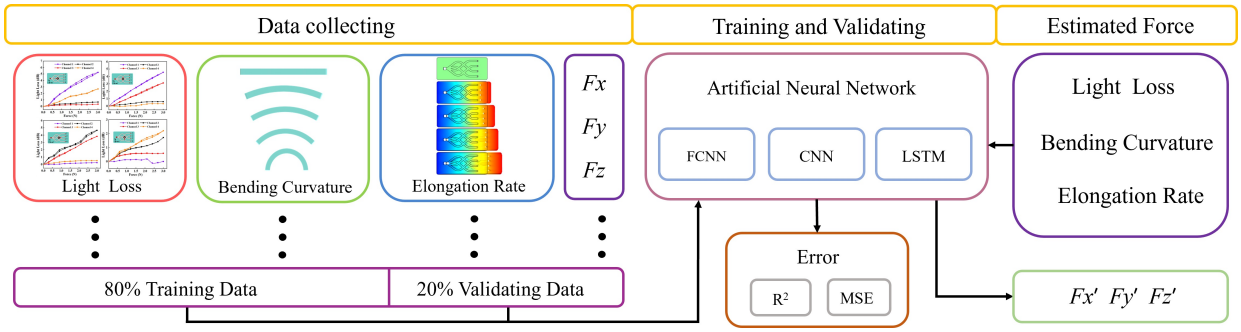

Fig. 8. Flowchart of the neural network training for estimating external forces based on sensor data. The process begins with data collection, including light loss, bending curvature, and elongation rates across various deformation modes. Data is split into 80% for training and 20% for validation. The neural networks, involving FCNN, CNN, and LSTM models, were used to predict the 3-axial forces F_x, F_y, and F_z. Performance was evaluated using R^2 and MSE metrics, ensuring accurate force estimation.

deformations, where traditional analytical models fall short. Initially, extensive data collection was undertaken, with bending radius ranging from 10mm to 60mm in 5mm increments, and elongation rates from 0% to 40% in 5% increments. Pressing experiments with force ranging from 0 to 3 N in 0.3 N increments were performed under bending, stretching, and combined deformation modes. Each force step lasted approximately 2 seconds, during which optical signals and 3-axis force data were synchronously sampled at 100 Hz. For each deformation condition, five repeated loading–unloading cycles were conducted to ensure statistical robustness and minimize random error. The flowchart for the neural network training process is illustrated in Fig. 8. The input features for the neural network model included elongation, bending curvature, and the light loss detected from four channels while the target outputs were the 3-axial force F_x, F_y, and F_z.

In the neural network training, we investigated three methodologies: Fully Connected Neural Network (FCNN), Convolutional Neural Network (CNN), and Long Short-Term Memory Network (LSTM). Their performance Was evaluated by assessing the linear fit (R^2), which indicates how well the regression line approximates the actual data points, the Mean Square Error (MSE%), which quantifies the average squared difference between predicted and actual values, as well as the magnitude and phase differences of the resultant force for each method, as detailed in Table 3.

The results demonstrate that the CNN outperforms both the FCNN and LSTM, achieving the lowest MSE of 0.00786 and the highest R^2 value of 0.98472, suggesting an excellent fit to the data. Furthermore, the CNN exhibits superior performance in terms of magnitude error, with the smallest error of 0.10058 N and a phase error of just 1.03539°. The findings demonstrate that the CNN method achieves high accuracy in predicting external forces across various deformation modes of the proposed sensor, underscoring its critical importance for practical applications.

TABLE III
PERFORMANCE COMPARISON OF DIFFERENT NEURAL NETWORK MODELS

Neural network	MSE	R^2	Magnitude Error (N)	Phase Error (°)
FCNN	0.05923	0.89929	0.25700	0.88745
CNN	0.00786	0.98472	0.10058	1.03539
LSTM	0.01019	0.98042	0.10912	0.99775

IV. Conclusion and Discussion

This paper introduces a novel, fully flexible optical-based 3-axial force sensor capable of adapting to curved and complex surfaces, achieving precise measurements of both force magnitude and direction by detecting output patterns from four intersecting optical waveguides. The research begins with a comprehensive analysis of the fundamental principles of optical waveguides, including intrinsic, extrinsic, and intersection losses, establishing a theoretical foundation for optimizing waveguide designs to minimize light loss. Following this, the sensor's design, working principles, and fabrication process are detailed, along with a thorough evaluation of its performance under various deformation modes such as stretching, pressing, and bending.

Experimental results demonstrated the sensor's exceptional performance, achieving a resolution of 0.0073 N and a hysteresis of 4.76%, thus confirming its reliability for force sensing across diverse deformation scenarios. Additionally, neural network methodologies, specifically a Convolutional Neural Network (CNN), were employed to model the relationship between force and light intensity, achieving highly accurate predictions with an R^2 value of 0.98472 and a force error of just 0.10058 N. In conclusion, the proposed sensor significantly advances existing tactile sensing technologies by offering precise 3-axial force measurement on complex, curved surfaces.

It should be noted that due to minor fabrication induced variations, such as molding tolerances and the presence of microbubbles or impurities in the elastomer, each fabricated sensor requires a separate calibration to establish its optical-force mapping accurately. However, since all sensors share identical structural and material parameters, the underlying relationship between optical attenuation and force components remains consistent across different devices. In practice, this enables the pre-trained CNN model to be efficiently fine-tuned for newly fabricated sensors through a transfer learning approach, thereby reducing calibration time and improving scalability for large scale deployment.

Future work will focus on optimizing the sensor design to achieve effective decoupling of multiple deformation modes, such as bending, stretching, and pressing. This may involve the introduction of additional optical variables, including the extraction of spectral information, to enhance the sensing dimensionality. Moreover, the impact of ambient or environmental light on sensor performance also needs to be systematically evaluated, and testing under varying illumination conditions, such as low light, fluorescent, and direct sunlight, will provide critical insights for real-world applications. Furthermore, distributed 3-axis force sensing across multiple contact points has not yet been realized, so increasing the number of sensing units and improving spatial resolution will be key directions. Finally, application evaluations in flexible systems and soft robotics will be conducted to validate the sensor's stability and robustness under practical conditions.

References

[1] W. Mandil, V. Rajendran, K. Nazari, and A. Ghalamzan-Esfahani, "Tactile-sensing technologies: Trends, challenges and outlook in agri-food manipulation," *Sensors*, vol. 23, no. 17, p. 7362, 2023.

[2] E. Liu, Z. Cai, Y. Ye, M. Zhou, H. Liao, and Y. Yi, "An overview of flexible sensors: Development, application, and challenges," *Sensors*, vol. 23, no. 2, p. 817, 2023.

[3] Y. Kim, A. Chortos, W. Xu, Y. Liu, J. Y. Oh, D. Son, J. Kang, A. M. Foudeh, C. Zhu, Y. Lee *et al.*, "A bioinspired flexible organic artificial afferent nerve," *Science*, vol. 360, no. 6392, pp. 998–1003, 2018.

[4] P. Wu, A. Xiao, Y. Zhao, F. Chen, M. Ke, Q. Zhang, J. Zhang, X. Shi, X. He, and Y. Chen, "An implantable and versatile piezoresistive sensor for the monitoring of human–machine interface interactions and the dynamical process of nerve repair," *Nanoscale*, vol. 11, no. 44, pp. 21 103–21 118, 2019.

[5] G. Shen, C. Zhang, T. Liang, Y. Xin, J. Liang, Y. Zhong, J. He, X. He, and X. He, "Microstructure engineering of stretchable resistive strain

sensors with discrimination capabilities in transverse and longitudinal directions," *Macromolecular Materials and Engineering*, vol. 306, no. 10, p. 2100283, 2021.

[6] B. Nie, R. Huang, T. Yao, Y. Zhang, Y. Miao, C. Liu, J. Liu, and X. Chen, "Textile-based wireless pressure sensor array for human-interactive sensing," *Advanced Functional Materials*, vol. 29, no. 22, p. 1808786, 2019.

[7] J. Yang, S. Luo, X. Zhou, J. Li, J. Fu, W. Yang, and D. Wei, "Flexible, tunable, and ultrasensitive capacitive pressure sensor with microconformal graphene electrodes," *ACS applied materials & interfaces*, vol. 11, no. 16, pp. 14 997–15 006, 2019.

[8] K. T. Fujimoto, J. K. Watkins, T. Phero, D. Litteken, K. Tsai, T. Bingham, K. L. Ranganatha, B. C. Johnson, Z. Deng, B. Jaques *et al.*, "Aerosol jet printed capacitive strain gauge for soft structural materials," *npj Flexible Electronics*, vol. 4, no. 1, p. 32, 2020.

[9] V. K. Rao, N. Shauloff, X. Sui, H. D. Wagner, and R. Jelinek, "Polydiacetylene hydrogel self-healing capacitive strain sensor," *Journal of Materials Chemistry C*, vol. 8, no. 18, pp. 6034–6041, 2020.

[10] X. Hu, X. Yan, L. Gong, F. Wang, Y. Xu, L. Feng, D. Zhang, and Y. Jiang, "Improved piezoelectric sensing performance of p (vdf–trfe) nanofibers by utilizing bto nanoparticles and penetrated electrodes," *ACS applied materials & interfaces*, vol. 11, no. 7, pp. 7379–7386, 2019.

[11] Z. Zhang, L. Chen, X. Yang, T. Li, X. Chen, X. Li, T. Zhao, and J. Zhang, "Enhanced flexible piezoelectric sensor by the integration of p (vdf-trfe)/agnws film with a-igzo tft," *IEEE Electron Device Letters*, vol. 40, no. 1, pp. 111–114, 2018.

[12] Z. Chen, Z. Wang, X. Li, Y. Lin, N. Luo, M. Long, N. Zhao, and J.-B. Xu, "Flexible piezoelectric-induced pressure sensors for static measurements based on nanowires/graphene heterostructures," *Acs Nano*, vol. 11, no. 5, pp. 4507–4513, 2017.

[13] S. Chen, J. Luo, X. Wang, Q. Li, L. Zhou, C. Liu, and C. Feng, "Fabrication and piezoresistive/piezoelectric sensing characteristics of carbon nanotube/pva/nano-zno flexible composite," *Scientific reports*, vol. 10, no. 1, p. 8895, 2020.

[14] Z. Liu, Y. Ma, H. Ouyang, B. Shi, N. Li, D. Jiang, F. Xie, D. Qu, Y. Zou, Y. Huang *et al.*, "Transcatheter self-powered ultrasensitive endocardial pressure sensor," *Advanced Functional Materials*, vol. 29, no. 3, p. 1807560, 2019.

[15] Y.-W. Cai, X.-N. Zhang, G.-G. Wang, G.-Z. Li, D.-Q. Zhao, N. Sun, F. Li, H.-Y. Zhang, J.-C. Han, and Y. Yang, "A flexible ultra-sensitive triboelectric tactile sensor of wrinkled pdms/mxene composite films for e-skin," *Nano Energy*, vol. 81, p. 105663, 2021.

[16] J. Tao, R. Bao, X. Wang, Y. Peng, J. Li, S. Fu, C. Pan, and Z. L. Wang, "Self-powered tactile sensor array systems based on the triboelectric effect," *Advanced Functional Materials*, vol. 29, no. 41, p. 1806379, 2019.

[17] Z. Ren, J. Nie, J. Shao, Q. Lai, L. Wang, J. Chen, X. Chen, and Z. L. Wang, "Fully elastic and metal-free tactile sensors for detecting both normal and tangential forces based on triboelectric nanogenerators," *Advanced Functional Materials*, vol. 28, no. 31, p. 1802989, 2018.

[18] J. C. Yeo, C. T. Lim *et al.*, "Emerging flexible and wearable physical sensing platforms for healthcare and biomedical applications," *Microsystems & Nanoengineering*, vol. 2, no. 1, pp. 1–19, 2016.

[19] X. Wang, Z. Li, and L. Su, "Soft optical waveguides for biomedical applications, wearable devices, and soft robotics: A review," *Advanced Intelligent Systems*, vol. 6, no. 1, p. 2300482, 2024.

[20] Y. Li, J. Hu, D. Cao, S. Wang, P. Dasgupta, and H. Liu, "Optical-waveguide based tactile sensing for surgical instruments of minimally invasive surgery," *Frontiers in Robotics and AI*, vol. 8, p. 773166, 2022.

[21] J.-S. Heo, J.-H. Chung, and J.-J. Lee, "Tactile sensor arrays using fiber bragg grating sensors," *Sensors and Actuators A: Physical*, vol. 126, no. 2, pp. 312–327, 2006.

[22] J. Guo, K. Zhao, B. Zhou, W. Ning, K. Jiang, C. Yang, L. Kong, and Q. Dai, "Wearable and skin-mountable fiber-optic strain sensors interrogated by a free-running, dual-comb fiber laser," *Advanced Optical Materials*, vol. 7, no. 12, p. 1900086, 2019.

[23] L. Massari, E. Schena, C. Massaroni, P. Saccomandi, A. Menciassi, E. Sinibaldi, and C. M. Oddo, "A machine-learning-based approach to solve both contact location and force in soft material tactile sensors," *Soft robotics*, vol. 7, no. 4, pp. 409–420, 2020.

[24] A. Leal-Junior, A. Frizera, and C. Marques, "A fiber bragg gratings pair embedded in a polyurethane diaphragm: Towards a temperature-insensitive pressure sensor," *Optics & Laser Technology*, vol. 131, p. 106440, 2020.

[25] Z. F. Zhang, X. M. Tao, H. P. Zhang, and B. Zhu, "Soft fiber optic sensors for precision measurement of shear stress and pressure," *IEEE Sensors Journal*, vol. 13, no. 5, pp. 1478–1482, 2013.

[26] C. Lyu, P. Li, J. Zhang, and Y. Du, "Fiber optic sensors in tactile sensing: A review," *IEEE Transactions on Instrumentation and Measurement*, 2025.

[27] K.-P. Lee, J. Yip, K.-L. Yick, C. Lu, L. Lu, and Q.-W. E. Lei, "A novel force-sensing smart textile: Inserting silicone-embedded fbg sensors into a knitted undergarment," *Sensors*, vol. 23, no. 11, p. 5145, 2023.

[28] C. Li, J. Tang, C. Cheng, L. Cai, and M. Yang, "Fbg arrays for quasi-distributed sensing: A review," *Photonic Sensors*, vol. 11, pp. 91–108, 2021.

[29] M. L. Preti, F. Bernabei, A. B. Nardin, and L. Beccai, "Triaxial 3d-channeled soft optical sensor for tactile robots," *IEEE Sensors Journal*, 2024.

[30] B. Aksoy, Y. Hao, G. Grasso, K. M. Digumarti, V. Cacucciolo, and H. Shea, "Shielded soft force sensors," *Nature communications*, vol. 13, no. 1, p. 4649, 2022.

[31] M. Ramuz, B. Tee, J. Tok, and Z. Bao, "Transparent, optical, pressure-sensitive artificial skin for large-area stretchable electronics." *Advanced materials (Deerfield Beach, Fla.)*, vol. 24, no. 24, pp. 3223–3227, 2012.

[32] A. Levi, M. Piovanelli, S. Furlan, B. Mazzolai, and L. Beccai, "Soft, transparent, electronic skin for distributed and multiple pressure sensing," *Sensors*, vol. 13, no. 5, pp. 6578–6604, 2013.

[33] H. Krauss and K. Takemura, "Stretchable optical waveguide sensor capable of two-degree-of-freedom strain sensing mediated by a semidivided optical core," *IEEE/ASME Transactions on Mechatronics*, vol. 27, no. 4, pp. 2151–2157, 2022.

[34] A. Heiden, D. Preninger, L. Lehner, M. Baumgartner, M. Drack, E. Woritzka, D. Schiller, R. Gerstmayr, F. Hartmann, and M. Kaltenbrunner, "3d printing of resilient biogels for omnidirectional and exteroceptive soft actuators," *Science Robotics*, vol. 7, no. 63, p. eabk2119, 2022.

[35] H. Zhao, K. O'brien, S. Li, and R. F. Shepherd, "Optoelectronically innervated soft prosthetic hand via stretchable optical waveguides," *Science robotics*, vol. 1, no. 1, p. eaai7529, 2016.

[36] H. Bai, S. Li, J. Barreiros, Y. Tu, C. R. Pollock, and R. F. Shepherd, "Stretchable distributed fiber-optic sensors," *Science*, vol. 370, no. 6518, pp. 848–852, 2020.

[37] E. Lee, S. Kim, and Y.-L. Park, "Multimodal soft optical waveguide sensor with microstructured core-cladding interface for human-robot interaction," *npj Robotics*, vol. 3, no. 1, p. 25, 2025.

[38] X. Yan, X. Yan, T. Zhang, M. Chen, Y. Luo, Z. Wang, Z. Qian, Z. Shang, T. Zhang, L. Wei *et al.*, "Soft and stretchable optical fibers with gradient color coding for multipoint bending and tactile perception in dexterous hands," *ACS sensors*, 2025.

[39] C. Jiang, Z. Zhang, J. Pan, Y. Wang, L. Zhang, and L. Tong, "Finger-skin-inspired flexible optical sensor for force sensing and slip detection in robotic grasping," *Advanced materials technologies*, vol. 6, no. 10, p. 2100285, 2021.

[40] M. S. Han and C. K. Harnett, "Soft, all-polymer optoelectronic tactile sensor for stick-slip detection," *Advanced Materials Technologies*, vol. 7, no. 12, p. 2200406, 2022.

[41] Y. Li, W. Gaozhang, J. Hu, D. Cao, P. Dasgupta, and H. Liu, "Optical-waveguide based 3-axial tactile sensor for minimally invasive surgical instruments," *IEEE Robotics and Automation Letters*, 2023.

[42] A. Ghatak and K. Thyagarajan, "Optical waveguides and fibers," *Fundamentals of Photonics*, vol. 2, pp. 269–292, 2000.

[43] C. Wilkinson, "Integrated optics: Theory and technology," *Optica Acta: International Journal of Optics*, vol. 30, no. 4, pp. 415–415, 1983.

[44] V. Sivashankar, E. McKenna, and A. Mickelson, "Guided wave optical components and devices," 2006.

[45] D. Calloway, "Beer-lambert law," *Journal of Chemical Education*, vol. 74, no. 7, p. 744, 1997.

[46] A. Snyder, "Optical waveguide theory," 1983.

[47] T. Kurokawa and S. Oikawa, "Optical waveguide intersections without light leak," *Applied Optics*, vol. 16, no. 4, pp. 1033–1037, 1977.

Yue Li She received her B.S. degree in Electrical Engineering from Xiamen University, China, in 2017, and her M.S. degree in Electrical Engineering from Xi'an Jiaotong University, China, in 2020. She obtained her Ph.D. degree in Biomedical Engineering from King's College London, UK. She is currently a Senior Research Fellow at University College London. Her research interests include haptic perception and soft robotics.

Wenlong Gaozhang (Student Member, IEEE) received a B.S. degree in Mechanical Engineering from Xiamen University, China, in 2017, and an M.S. degree in Mechanical Engineering from Xi'an Jiaotong University, China, in 2020. He is currently pursuing a PhD degree in Mechanical Engineering at University College London, London, UK. His research interests include soft robotics and collaborative robots.

Jian Hu is with State Key Laboratory of Multimodal Artificial Intelligence Systems, Institute of Automation, Chinese Academy of Sciences, Beijing, China, and Centre for Artificial Intelligence and Robotics, HK Institute of Science & Innovation, Chinese Academy of Sciences, Hong Kong SAR, China. His research focuses on the development of medical robotic systems with advanced haptic perception.

Gongyu Zhang (Student Member, IEEE) received his B.S. degree from Xi'an Jiaotong-Liverpool University and the University of Liverpool in 2018, and his M.S. degree from University College London in 2019. He is currently a Research Fellow at King's College London and an affiliated researcher at the UCL Institute of Ophthalmology and Moorfields Eye Hospital, London, UK. His research interests focus on computer vision, medical image analysis, and the application of deep learning techniques in ophthalmology.

Prokar Dasgupta is a clinician-scientist and professor of surgery at the Surgical Academy of King's Health Partners. Since 2002, he has served as a consultant urologist at Guy's Hospital. In 2009, he became the first professor of robotic surgery and urology at King's College and later chaired the King's College-Vattikuti Institute of Robotic Surgery. He was chief investigator for the world's first randomized controlled trial of telerobotics and the only trial comparing open, laparoscopic and robotic cystectomy.

Sebastien Ourselin (Member, IEEE) is Head of the School of Biomedical Engineering and Imaging Sciences at King's College London, which is dedicated to the development, clinical translation and clinical application of medical imaging, computational modelling, minimally invasive interventions and surgery. He is Director of the Wellcome / EPSRC Centre for Interventional and Surgical Sciences and the EPSRC Image-Guided Therapies UK Network+. He has published over 400 articles and is an associate editor for IEEE Transactions on Medical Imaging, Journal of Medical Imaging, Nature Scientific Reports, and Medical Image Analysis.

Hongbin Liu is a Professor at Chinese Academy of Sciences, Institute of Automation (CASIA), Executive Deputy Director for the Centre of AI and Robotics (CAIR), Hong Kong Institute of Science and Innovation, Chinese Academy of Sciences. Dr Liu is also an adjunct Reader and director of the Haptic Mechatronics and Medical Robotics (HaMMeR) lab at the School of Biomedical Engineering and Imaging Sciences, King's College London (KCL), UK. Dr Liu's group has been focusing on research and development of medical robotic systems with advanced haptic perception and interaction capabilities, to enable safer and more effective minimally invasive diagnosis and treatment for patients. Dr Liu's research has led to the clinical translation of a series of flexible robotic endoscopic systems for applications such as colonoscopy, bronchoscopy as well as vascular surgeries.